arXiv:cond-mat/0207731v1 [cond-mat.dis-nn] 31 Jul 2002

Avalanche Dynamics in Wet Granular Materials

P. Tegzes,[1,2] T. Vicsek,[2] and P. Schiffer[1]

[1]*Department of Physics and Materials Research Institute, Pennsylvania State University, University Park PA 16802*

[2]*Department of Biological Physics, Eötvös Loránd University, 1A Pázmány sétány, Budapest, Hungary 1117*

(Dated: March 22, 2022)

A detailed characterization of avalanche dynamics of wet granular media in a rotating drum apparatus is presented. The results confirm the existence of the three wetness regimes observed previously: the granular, the correlated and the viscoplastic regime. These regimes show qualitatively different dynamic behaviors which are reflected in all the investigated quantities. We discuss the effect of interstitial liquid on the characteristic angles of the material and on the avalanche size distribution. These data also reveal logarithmic aging and allow us to map out the phase diagram of the dynamical behavior as a function of liquid content and flow rate. Via quantitative measurements of the flow velocity and the granular flux during avalanches, we characterize novel avalanche types unique to wet media. We also explore the details of viscoplastic flow (observed at the highest liquid contents) in which there are lasting contacts during flow, leading to coherence across the entire sample. This coherence leads to a velocity independent flow depth at high rotation rates and novel robust pattern formation in the granular surface.

PACS numbers: 45.70.-n, 45.70.Ht, 45.70.Mg

INTRODUCTION

While most research on the physics of granular media has focused on dry grains, the presence of even microscopic quantities of interstitial liquid can have profound effects on the physical behavior [1, 2, 3, 4, 5, 6, 7, 8, 9]. Capillary forces lead to cohesion which greatly enhances the stability of wet samples, and several recent studies have investigated liquid induced effects on the static properties [2, 3, 4, 5, 6, 7]. In previous studies of the repose angle of wet granular media using a draining crater apparatus [10], we identified three fundamental regimes as a function of the liquid content. The *granular regime* at very low liquid contents is dominated by the motion of individual grains; in the *correlated regime* corresponding to intermediate liquid contents, a rough surface is formed by the flow of separated clumps; and the repose angle of very wet samples results from smooth, cohesive flow with *viscoplastic* properties. The addition of liquid also qualitatively changes the dynamic behavior of granular media, as was observed qualitatively in our angle of repose measurements and also revealed in recent segregation studies [8, 9]. A quantitative characterization of the *dynamics* of wet granular flow, however, has thus far been missing. In this paper we study the avalanche dynamics and flow properties of wet granular materials to investigate how the gradual addition of a small amount of liquid influences the dynamic properties of granular surface flow, and we find that the three fundamental regimes observed earlier are also reflected in the present experiment. Some of the results presented here have been published elsewhere [11].

Granular surface flow occurs when the inclined surface of a granular medium loses its stability against gravitational force. There are several experimental methods to investigate such flow, e.g. by gradually tilting a granular sample, which leads to an avalanche when the surface angle exceeds a critical value $\theta_{\max}$ [12]. Alternatively, if the surface angle is close to $\theta_{\max}$, avalanches can be triggered by point-like perturbations [13]. The inclination of the surface can also be increased by the addition of grains to the top of the pile [14, 15] or by slowly decreasing the size of the supporting base [16].

In our measurements we employ a rotating drum apparatus (a cylindrical chamber partly filled with a granular medium and rotated around a horizontal axis) [17, 18], which tilts the sample in a highly controlled and reproducible manner and offers several benefits. The most important advantage of a rotating drum is that at low rotation rates it allows for the observation of many avalanches without the need to change the sample. After each avalanche the medium remains at rest relative to the drum while its surface angle is slowly increased by rotation, until it reaches $\theta_{\max}$ again. Then another avalanche occurs, and the process starts over. Thus it is possible to record hundreds of avalanches, which is essential for performing a statistical analysis or for averaging out noise-like fluctuations in dynamical data. In addition to the avalanches observed at low rotations rates, the rotating drum also allows the investigation of continuous flow down the slope at higher rotation rates.

The sections of this paper cover different aspects of our rotating drum experiments. In Section we describe the experimental setup. Section addresses some issues explored in previous studies of cohesive granular media in a rotating drum [6, 19, 20, 21], focussing on the surface angles of the medium before and after avalanches, and describing a statistical analysis of avalanche size based on these angles. In Section we investigate the transition

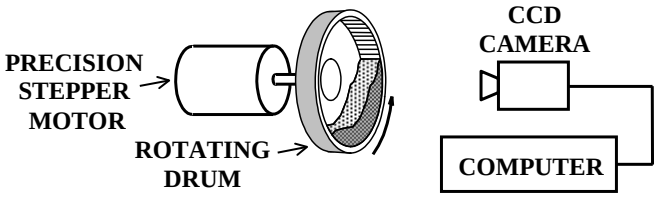


FIG. 1: Sketch of the experimental setup.

between avalanches and continuous flow as a function of the liquid content, and map out the phase diagram of the system. Then a short section () is devoted to the morphology of the surface. In the rest of the paper we focus on characterizing the *dynamics of cohesive flow*. In Section we quantitatively investigate the flow dynamics during avalanches at different liquid contents by analyzing the time evolution of the averaged surface profile obtained from hundreds of avalanche events. In Section we analyze the dynamical properties of the continuous flow phase occurring at faster rotation. We pay special attention to the nature of the *viscoplastic* flow, observed at the highest liquid contents which displays unique characteristics associated with coherent motion over the entire granular surface. In the final section we summarize and discuss our results.

DESCRIPTION OF THE APPARATUS

We studied glass spheres thoroughly mixed with small quantities of hydrocarbon oil. The viscosity of the oil used was 0.27 poise, and its surface tension was $0.02\,\mathrm{N/m}$. The liquid content varied between $\tau = 0.001\,\%$ and $5\,\%$ of the void volume. In this regime the flow of oil due to gravity can be neglected. Measurements were performed on three sizes of beads, with diameters $d = 0.9\,\mathrm{mm} \pm 11\,\%$, $d = 0.5\,\mathrm{mm} \pm 20\,\%$ and $d = 0.35\,\mathrm{mm} \pm 15\,\%$. Note the the beads differed not only in their size, but also presumably in their microscopic surface structures, which are difficult to characterize or control. Nonetheless, most of the qualitative behavior is reproduced in the different grain samples, those differences which are significant are mentioned below.

The rotating drum (Fig. 1) was made of thick plexiglas, but the vertical walls were lined with glass plates in order to minimize electrostatic effects. To prevent slips along the circumference of our drum, we inserted a hollow, thin aluminum cylinder with a rough inner surface into the drum. The inner diameter of the drum was 16.8 cm, its width was 3.2 cm, and the granular filling was 30 %. By performing measurements in a thinner (2 cm) drum we verified that, while wall effects are not negligible, they do not appear to modify the qualitative behavior.

The drum was rotated by a computer-controlled precision stepping motor which provided an extremely stable rotation rate that could be varied in the range of $\approx 0.003 - 30$ rotation per minute (rpm). The step size of rotation was 0.025°. The vibrations originating from the stepper motor were damped by multiple lead bricks attached to the apparatus.

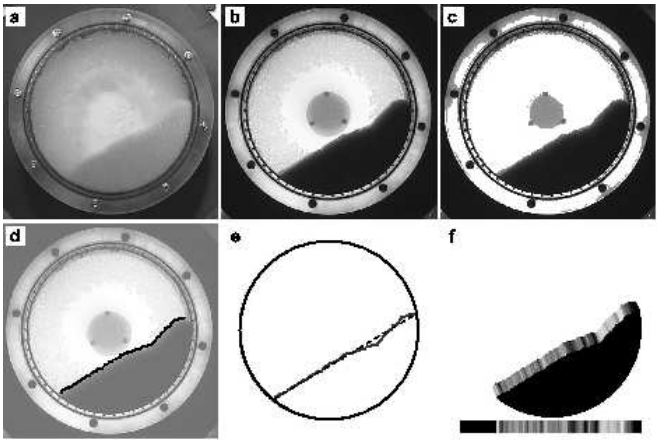


FIG. 2: *This is a reduced resolution figure* [22]. Steps of image processing. (a) Snapshot taken without background illumination. The wet grains sticking to the glass walls make the surface profile hardly visible. (b) The same picture but with a circular lamp turned on in the background. In diffuse background illumination the monolayer of beads on the wall is much brighter than the 3.2 cm thick sample. (c) A brightness threshold is applied to the image to make the beads on the walls disappear. (d) Test of the algorithm: the surface data (black line) superimposed over a greyed version of the original photograph. (e) The surface profile with a fitted straight line determining the overall surface angle (θ). (f) Pseudo-3dimensional representation of the surface profile, shading indicates local angle ($\alpha(x)$). This shading may be used to represent a given surface profile in a single line (see the horizontal stripe at the bottom).

The experiment was recorded by a charge coupled device video camera interfaced to a computer which could analyze the spatiotemporal evolution of the surface profile (height variations in the axial direction were negligible). The steps of image processing are demonstrated in Fig. 2(a-c). When the grains are wet, the beads sticking to the glass walls make the surface hardly visible (Fig. 2(a)). We overcame this problem by using background illumination (Fig. 2(b)) and applying a brightness threshold (Fig. 2(c)) on the image. We found the surface profile $h(x)$ by an algorithm based on the detection of points of maximum contrast [23]. The resulting surface data are presented in Fig. 2(d-f) in different ways. Fig. 2(d) shows a test of the algorithm: the detected surface is superimposed on the photograph of the system as a thin black line. The limitations of our camera and computer gave us a resolution of $\delta t = 0.03$ seconds and $\delta x = 0.5\,\mathrm{mm}$. Fig. 2(e) presents the $h(x)$ curve together with a straight line that was fitted to the curve in a rotation-invariant way: the squared sum of the *geometrical distances* of the sur-

face point from the line was minimized. The inclination angle of this line gives the *overall angle* of the surface. This is the generalized version of the surface angle that has typically been used to describe the flat surface of dry samples. Finally, Fig. 2(f) shows the surface profile with a brightness-coded representation of the local angle ($\alpha(x) = \arctan\left[\frac{d}{dx}h(x)\right]$) in the third dimension. The stripe at the bottom is a concise way of displaying this surface profile using the same shading. In sections and we use this representation of the surface topography to visualize the time evolution of the surface by placing the stripes corresponding to successive surface profiles under each other.

DYNAMIC PROPERTIES FROM SURFACE ANGLE MEASUREMENTS

The phenomenology of wet granular materials is much richer than that of dry samples. The attractive forces between the particles lead to correlated motion of the grains and qualitatively new avalanche dynamics. These new types of avalanches form rough and highly variable surfaces. In order to capture the most fundamental features of our system, however, we will initially neglect these surface features and examine only the *overall surface angle* (Fig. 2(e)) to describe the observed surfaces with a single number. This approach allows us to compare our results directly to the behavior of dry materials, where the surface is virtually flat and is completely described by its inclination angle.

Fig. 3 shows the time evolution of the surface angle for various rotation rates. Similarly to the dry materials we observe discrete avalanches at low rotation rates. We find that $\theta(t)$ in this regime is a typical sawtooth-shaped function looking very similar to the force-displacement curve of stick-slip processes, which is not very surprising since stick-slip-like behavior is quite frequent in granular materials [24, 25, 26, 27]. The local maximum and minimum points of $\theta(t)$ correspond to the maximum angle of stability ($\theta_{\max}$) and the repose angle (θ_r) respectively. Note, that if we plot the surface angle as a function of the rotation angle of the drum, then the increasing segments of the curve are straight lines with a slope of unity. If we gradually increase the angular velocity of the drum, then at a given rotation rate ($\Omega = 4\,$rpm in Fig. 3) the flow becomes continuous, and after some transients the surface angle becomes constant. In this section we consider the avalanching regime (at $\Omega = 0.12\,$rpm, except where noted otherwise) and investigate how the characteristic angles and the avalanche size distribution depends on the liquid content and the rotation rate. The transition to continuous flows is described in the subsequent section.

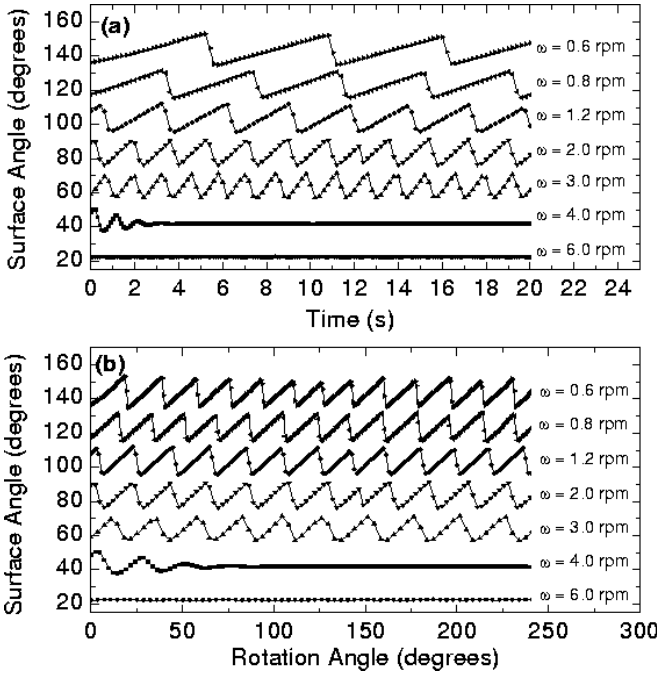


FIG. 3: *This is a reduced resolution figure* [22]. The temporal variation of the surface angle at various rotation rates (a) as a function of time, (b) as a function of the rotation angle of the drum. These data were taken using the large $d = 0.9\,$mm beads, the liquid content was $\tau = 0.009\,\%$. Note that the curves are shifted by increments of 20° for clarity.

The maximum and the repose angle

Fig. 4 shows the maximum angle just before an avalanche, $\langle\theta_{\max}\rangle$, and the angle of repose after an avalanche, $\langle\theta_r\rangle$, as a function of liquid content for the three different bead sizes (averaged over several hundred avalanches). The measured angles have distributions of finite width, the error bars in the figure indicate their standard deviation. These characteristic angles reveal essential properties of the material: $\theta_{\max}$ reflects the stability of the sample while θ_r is also related to the dissipation during the avalanche events. The various features of these curves reflect changes in the dynamical behavior corresponding to the three regimes mentioned in the introduction, which are described in this section through qualitative observations, and are more quantitatively characterized in Section .

The curves corresponding to the smaller bead sizes $d = 0.5\,$mm (Fig. 4(b)) and $d = 0.35\,$mm (Fig. 4(c)) are quite similar. At the lowest liquid contents, very small avalanches are observed. This is the granular regime, where the behavior is qualitatively similar to that of dry granular materials. Due to the interparticle cohesive forces, $\theta_{\max}$ in this regime is larger than the value measured in dry samples. On the other hand, θ_r hardly changes, presumably because the presence of interstitial liquid does not significantly alter the dissipation in the

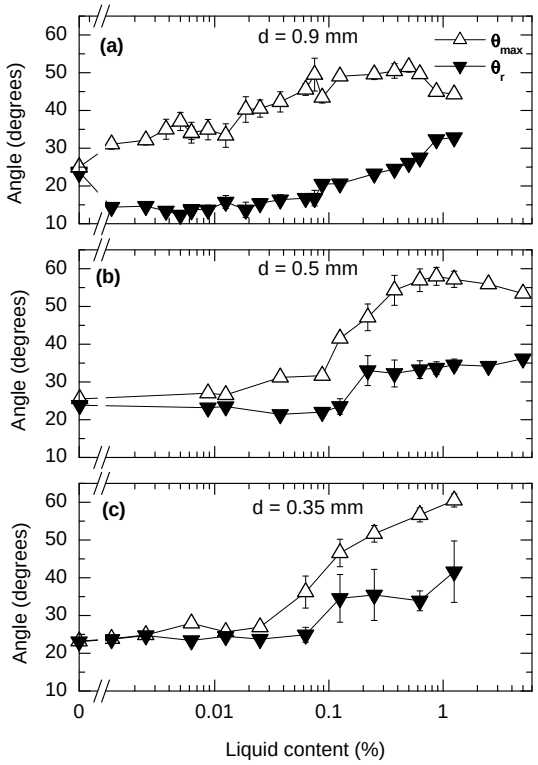


FIG. 4: The dependence of the maximum angle $\theta_{\max}$ and the repose angle θ_r on the liquid content for 3 different bead sizes. (a) $d = 0.9\,\mathrm{mm}$, $\Omega = 0.12\,\mathrm{rpm}$, (b) $d = 0.5\,\mathrm{mm}$, $\Omega = 0.12\,\mathrm{rpm}$, (c) $d = 0.35\,\mathrm{mm}$, $\Omega = 0.03\,\mathrm{rpm}$ (a lower rotation rate was chosen, because at $\Omega = 0.12\,\mathrm{rpm}$ the smallest beads exhibit continuous flow for the lowest liquid contents).

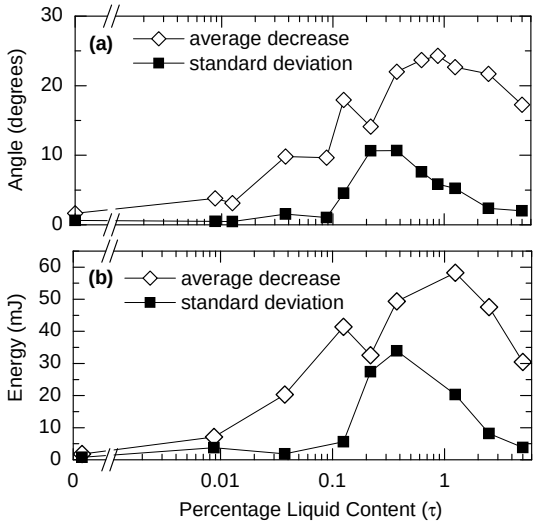


FIG. 5: The average avalanche size and the width of the avalanche size distribution as a function of liquid content, calculated with two different methods. (a) Decrease in the surface angle: $\langle\Delta\theta\rangle$, $2\sigma(\Delta\theta)$, (b) Decrease in the potential energy: $\langle\Delta E\rangle$, $2\sigma(\Delta E)$. The data were taken using medium size beads, $d = 0.5\,\mathrm{mm}$, $\Omega = 0.12\,\mathrm{rpm}$.

fluidized layer of rolling beads.

At higher liquid contents, in the correlated regime, the increased cohesive force results in a larger increase in $\theta_{\max}$. In this regime the beads on the top surface are more effectively stabilized by the cohesive forces, thus failure leading to an avalanche occurs in the bulk of the sample, and the avalanche flow includes the motion of correlated clumps. We find that θ_r also displays a sudden increase, but at somewhat higher liquid contents than the increase in $\theta_{\max}$. This offset is possibly due to the motion of the clump fluidizing the underlying layer of beads, thus individual rolling grains help determine the final slope as in the granular regime. At higher liquid contents, the cohesive and viscous forces would prevent such fluidization leading to the increase in θ_r.

At the highest liquid contents, $\theta_{\max}$ slightly decreases in Fig. 4(a) and (b). This decrease in the stability of the material, also observed in our previous studies of the repose angle using a different technique [10], is probably related to lubrication effects decreasing the static friction among the grains. In this regime the nature of the avalanches changes again: the material is transported by coherent flow extending over the whole surface of the sample. We did not observe this regime for the $d = 0.35\,\mathrm{mm}$ beads, possibly because, for those grains, the cohesive forces are much stronger relative to their weight. Careful examination of Fig. 4 reveals a few other differences between the different grains studied such as the relatively large avalanches exhibited by the $d = 0.9\,\mathrm{mm}$ beads even at very low liquid contents. These differences are difficult to interpret, since we only examined three grain samples which varied not only in their size, but presumably also in their microscopic surface properties.

Statistics of avalanche sizes

Thus far we have restricted our discussion to the average values $\langle\theta_{\max}\rangle$ and $\langle\theta_r\rangle$. However, the characteristic angles are influenced by the microstructure of the sample, i.e., the actual configuration of the grains, which leads to inherent fluctuations and a non-trivial distribution of the measured quantities. The analysis of these distributions may provide insight into the internal dynamics of the material. In particular the statistics of avalanche sizes has attracted much recent attention due to its possible connection to self organized criticality [14, 16, 17, 18, 21, 28, 29, 30].

In this section, we analyze the statistical distribution of avalanche sizes. The simplest quantity that describes the size of an avalanche is $\Delta\theta = \theta_{\max} - \theta_r$, which has been widely used to characterize avalanches among dry grains in a rotating drum [17, 31]. In Fig. 5(a) we plot

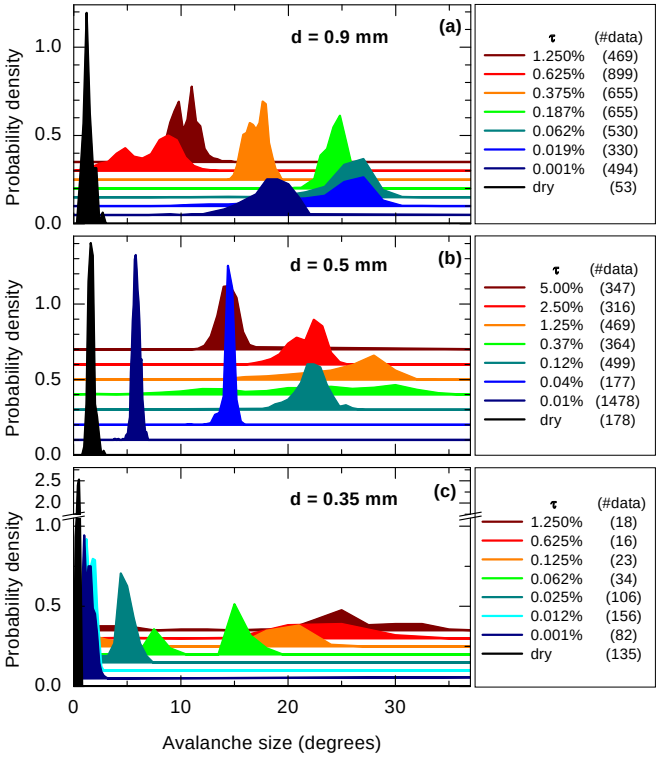


FIG. 6: (color) Distribution of the avalanche size ($\Delta\theta$) for various liquid contents. (a) Large beads, $d = 0.9\,\mathrm{mm}$, $\Omega = 0.12\,\mathrm{rpm}$, (b) medium beads, $d = 0.5\,\mathrm{mm}$, $\Omega = 0.12\,\mathrm{rpm}$, (c) small beads, $d = 0.35\,\mathrm{mm}$, $\Omega = 0.03\,\mathrm{rpm}$. The righthand column shows the number of avalanches included for each sample - note that the statistics are much better for the large and medium beads than for the smaller beads.

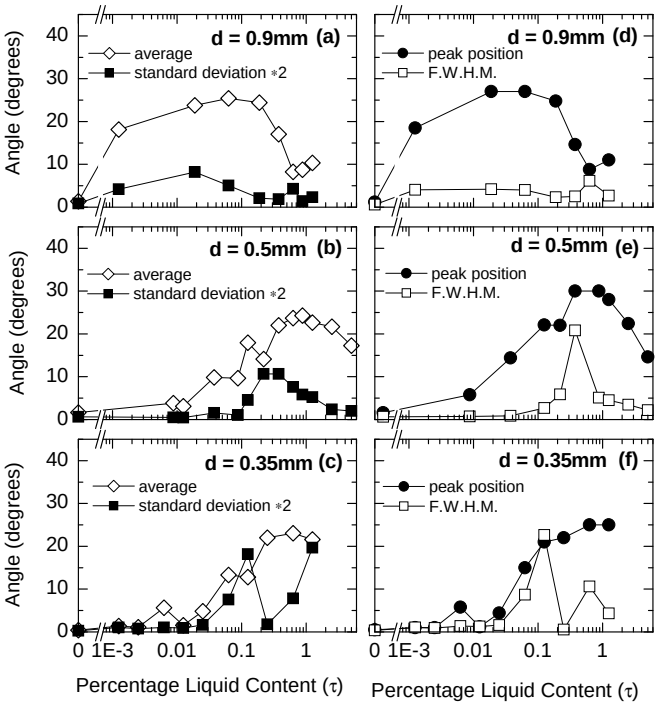


FIG. 7: Statistical measures of the avalanche size distributions presented in Fig. 6, for the 3 different bead sizes as indicated in the figure. (a-c) The average angle drop: $\langle\Delta\theta\rangle$, and the standard deviation $2\sigma(\Delta\theta)$ (see text). (d-f) The most probable avalanche size, *i.e.* the maximum of $P(\Delta\theta)$ ("peak position"), and the width of the peaks (full width at half maximum, "F.W.H.M.").

the average avalanche size

$$\langle\Delta\theta\rangle = \frac{1}{N}\sum_{i=1}^{N}\Delta\theta_i \qquad (1)$$

(where $\Delta\theta_i$, $i = 1..N$ is the angle drop in the i^{th} avalanche) and the width of the avalanche size distribution

$$\sigma(\Delta\theta) = \sqrt{\frac{N\sum_{i=1}^{N}\Delta\theta_i^2 - (\sum_{i=1}^{N}\Delta\theta)^2}{N(N-1)}} \qquad (2)$$

for the $d = 0.5\,\mathrm{mm}$ beads. (Note that we do not assume that the distribution is Gaussian, we just use the standard deviation as a measure of the width of the distribution.) Since the definition of the surface angle is somewhat arbitrary in the case of our surfaces which can be both rough and have global curvature (as discussed below), we also define an alternative measure of the avalanche size, ΔE, which equals the difference in the potential energy of the sample just before and just after the avalanche [32]. The analogous quantities $\langle\Delta E\rangle$ and $2\sigma(\Delta E)$ are plotted in Fig. 5(b). The graphs indicate that the two different measures of the avalanche size yield almost equivalent results, thus we use the standard $\Delta\theta$ as the measure of the avalanche size in the following discussion. In order to characterize the distribution in more detail, in Fig. 6 we plot the measured probability densities $P(\Delta\theta)$ for several liquid contents for the 3 different bead sizes, where $P(\Delta\theta)d\theta$ is the probability for the avalanche size to fall between $\Delta\theta$ and $\Delta\theta + d\theta$ (we estimate $P(\Delta\theta)$ from histograms). In Fig. 7 we also plot several statistical measures characterizing these distributions including the peak position (the maximum of $P(\Delta\theta)$) and the FWHM (full width of the peak at half of the maximum value).

The statistical properties of the avalanches shown in Fig. 6 and Fig. 7 exhibit several interesting features. The size of the typical avalanche quickly increases with increasing liquid content reflecting the increasing cohesion, then a decrease is observable when the viscoplastic regime is reached. At the lowest liquid contents we observe single peaks, i.e. the system has a characteristic avalanche size with noise-like variations. At larger liquid contents, however, in several cases we observe double peaks or extremely broad avalanche size distributions. This implies the existence of two or more characteristic avalanche sizes, i.e. both small and large avalanches may occur. A similar feature has been observed in fine cohe-

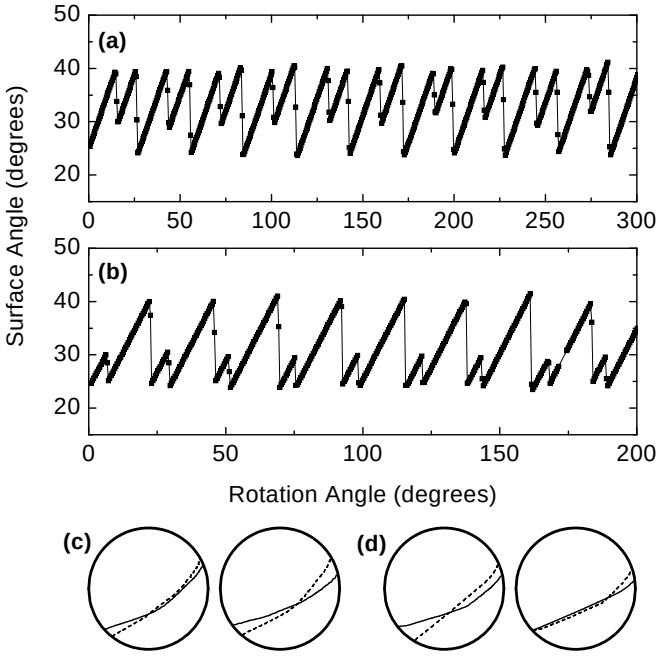


FIG. 8: Alternating small and large avalanches. (a) $d = 0.5\,\mathrm{mm}$, $\tau = 0.125\,\%$, $\Omega = 0.4\,\mathrm{rpm}$, (b) $d = 0.35\,\mathrm{mm}$, $\tau = 0.062\,\%$, $\Omega = 0.15\,\mathrm{rpm}$. (c) and (d) The initial (dashed line) and final (solid line) surface profiles for two successive avalanches. The parameters are the same as in (a) and (b) respectively. Unfortunately, due to the fluctuations in the system these patterns of behavior were difficult to create reproducibly.

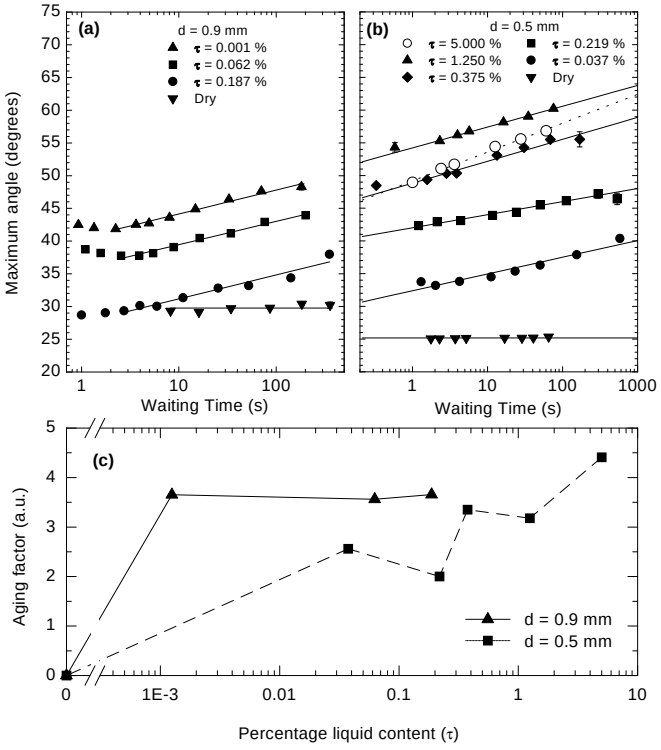


FIG. 9: (a-b) The dependence of the maximum angle $\theta_{\max}$ on the waiting time between successive avalanches. The system exhibits aging: longer waiting times between avalanches leads to increased stability. The continuous lines are logarithmic fits to the data. (a) $d = 0.9\,\mathrm{mm}$, (b) $d = 0.5\,\mathrm{mm}$. (c) The intensity of aging (i.e. the slope of the fitted straight lines in (a) and (b)) as a function of liquid content for the two different bead sizes.

sive powders [21]. As discussed below, this phenomenon is related to the fact that at high liquid contents the surface is far from being flat and both the limit of stability and the size of the avalanche depend strongly on the shape of the actual surface.

Within a rotating drum experiment, the initial condition for an avalanche is the surface profile formed by the previous avalanche. The shapes of the surfaces after successive avalanches can thus be regarded as steps of a special dynamical map. In the granular regime the freely rolling grains always smooth out the surface, so this mapping is trivial. However, in the correlated regime, where the existence of clumps leads to rugged surfaces, this map is rather complex. Due to the inherent fluctuations in the system, in most cases this mapping is stochastic, smaller and larger avalanches follow each other in a largely random manner. In some cases, however, the system reaches quasi-stable fixed points (when all the avalanches are very similar and their initial and final surfaces are rotated versions of each other), or limit cycles, when the initial profile is recovered in two or more avalanches. Two examples for this latter case are shown in Fig. 8. Unfortunately the fluctuations in our system usually destroy regular behavior, and thus we could not perform a detailed investigation of this map. But we expect that a corresponding model system without strong fluctuations would display an extremely rich chaotic behavior.

Logarithmic aging

As expected from previous studies, and shown in Section , $\theta_{\max}$ strongly depends on the liquid content due to the increasing capillary forces. Our measurements indicate that $\theta_{\max}$ also depends on the rotation rate, Ω. Although (for small Ω) the rotation rate only influences the waiting time between successive avalanches, $\theta_{\max}$ clearly decreases with increasing rotation rate. This effect (which is also visible in the measurements of the surface as a function of drum rotation rate shown below) is presented in Fig. 9(a) and (b), which show $\theta_{\max}$ as a function of the waiting time, i.e. the time between avalanche events which decreases with increasing rotation rate. The curves indicate a logarithmic increase in the stability of the system. In Fig. 9 (c) we also present the intensity of the aging process (quantified as the slope of the fitted straight lines). We do not observe aging for the dry samples, and the effect is somewhat stronger for

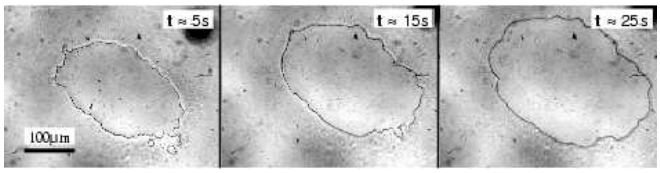


FIG. 10: *This is a reduced resolution figure* [22]. The oil at the contact point of a wet bead (similar to the ones used in the experiment, but $d = 1.2\,\mathrm{mm}$) and the glass plate on which it rests. The images are taken from above at different time instants via phase-contrast microscopy. The delay time from the instant when the bead was placed on the plate was (a) $t \approx 5\,\mathrm{s}$, (b) $t \approx 15\,\mathrm{s}$, (c) $t \approx 25\,\mathrm{s}$. The flow of oil to the contact point thus occurs on a timescale of several seconds, suggesting a natural explanation for our observed aging effects.

the larger liquid contents, though on the basis of our data we cannot determine the exact functional form.

Similar aging effects have been observed in several different granular experiments [6, 33], but the underlying mechanisms are complex, since several factors may play an important role [33]. Since in our experiment the effect is more pronounced at higher liquid contents, and the vapor pressure of oil is low, we attribute it to the motion of oil flowing towards the contact points rather than condensation effects [6]. This assumption is also supported by our investigations of a wet contact by phase contrast microscopy. We placed a wet bead on the object plate and observed a flow of oil to the region of the contact point (Fig. 10). Our observations revealed that a liquid bridge was formed instantaneously when the bead was placed on the plate, but the bridge's shape continued changing slowly even after several seconds of waiting time. This finding further supports the importance of viscosity to the stability of wet granular media which was demonstrated by Samandani et al. [8, 9].

THE ROLE OF THE ROTATION RATE: AVALANCHES AND CONTINUOUS FLOW

Hysteresis in the transition between continuous and avalanching flow

As mentioned above, if the rotation rate is increased above a threshold the system exhibits continuous flow instead of discrete avalanches. Earlier studies in dry media revealed that the transition between avalanching and continuous flow is hysteretic in rotation rate [17, 34]. Now we have investigated the avalanching – continuous flow transition for various liquid contents. We slowly increased and then decreased the rotation rate and measured the average surface angle in the continuous regime as well as $\theta_{\max}$ and θ_r in the avalanching regime. The rotation rate was changed in discrete steps by factors between 1.2 and 1.4, each step was performed with a constant angular acceleration in 3 seconds. Between the steps the drum was rotated for typically $0.5 - 1$ full rotation to determine whether the flow is continuous or avalanching (the minimum rotation was 90° at some of the lowest rotation rates, the maximum was 40 full rotations at $\Omega = 30\,\mathrm{rpm}$). We consider the flow continuous when the medium never comes to rest with respect to the drum, which coincides with $\Delta\theta \equiv \theta_{\max} - \theta_r < 1°$. The results of typical runs are presented in Fig. 11(a), (b) and (c), where $\theta_{\max}$ and θ_r are plotted as a function of the rotation rate.

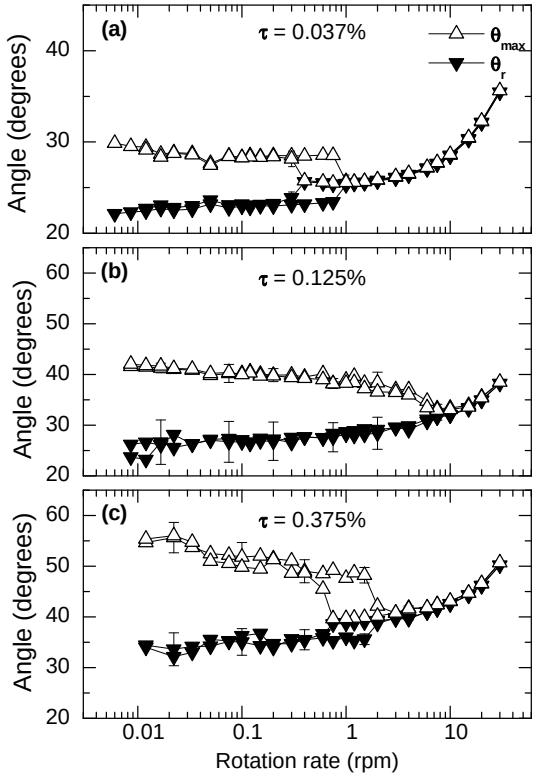


FIG. 11: (a) (b) (c) $\theta_{\max}$ and θ_r as a function of rotation rate for 3 different liquid contents, $d = 0.5\,\mathrm{mm}$. The error bars represent the standard deviation of the observed angle distributions.

The three basic regimes of behavior observed previously are also reflected in the nature of the transition. In the granular regime at low liquid contents, (e.g. $\tau = 0.037\,\%$), where the behavior is qualitatively similar to the dry case, we observe a clear hysteretic transition between continuous flow and avalanching (Fig. 11(a)). At a somewhat higher liquid content ($\tau = 0.125\,\%$, see Fig. 11(b)) the correlated behavior is marked by a lack of hysteresis, and intermittent avalanches are observed at a relatively high rotation rate compared to the other

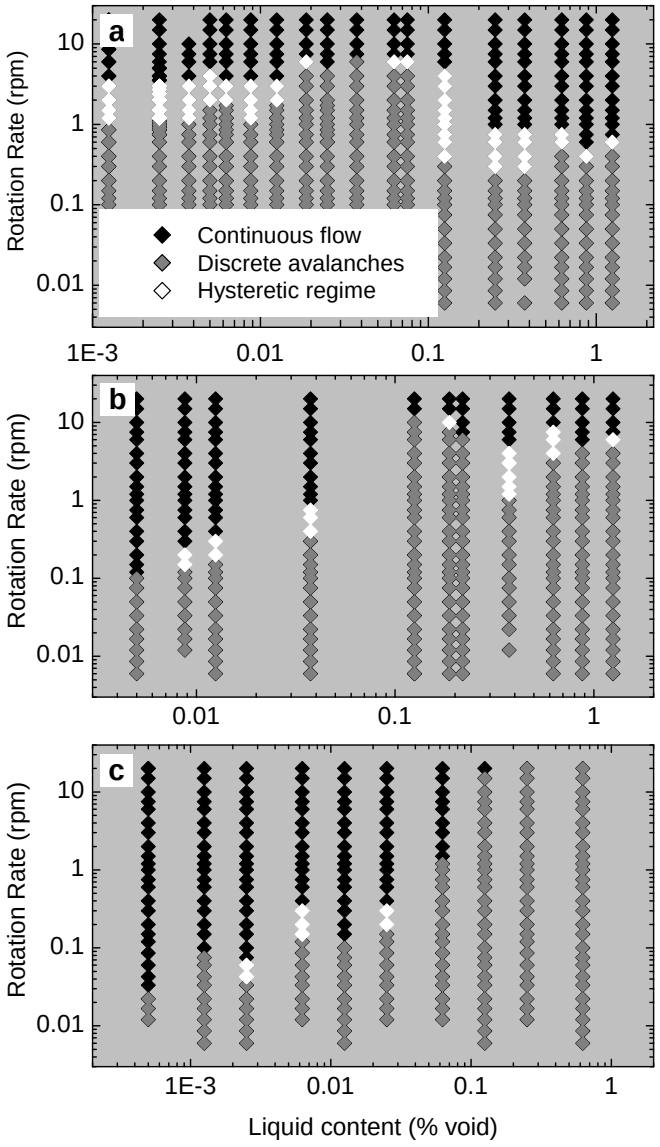


FIG. 12: (a) Phase diagram of the dynamical behavior as a function of the liquid content (τ) and the rotation rate (Ω). (a) large beads, $d = 0.9\,\mathrm{mm}$, (b) medium beads, $d = 0.5\,\mathrm{mm}$, (c) small beads, $d = 0.35\,\mathrm{mm}$.

regimes. The continuous flow in this regime consists of a stream of separated clumps rather than the constant flux seen in the other two regimes. At $\tau = 0.375\,\%$ (Fig. 11(c)) hysteresis is again observed, coinciding with the onset of the viscoplastic continuous flow, which is smooth and coherent over the entire sample.

The origin of the hysteresis in the transition between continuous and avalanching flow is a fascinating subject [17, 34, 35, 36], but a detailed discussion goes beyond the scope of this paper. We hypothesize that the hysteresis is observed because the transitions on increasing and decreasing rotation rate have different origins, thus they do not necessarily coincide. A rough explanation of the transition from avalanching to continuous flow is that the successive avalanches merge. More precisely, at high velocities the rotation during the avalanche is becoming important and the constant energy supply prevents the grains from stopping. For the reverse transition, the continuous flow cannot be maintained at arbitrarily low velocities, because then the flowing layer cannot stay fluidized, and the grains get stuck in small depressions of the underlying layer.

The nature of the transition is naturally different in the different wetting regimes. In the granular and the viscoplastic regime the constant material flux in the continuous flow phase is qualitatively different from the first increasing and then decreasing flux observed in the case of an avalanche. Thus the intermittent and the continuous flow may represent two locally stable dynamical phases with a hysteretic transition between them. On the other hand in the correlated regime there is no qualitative change in the flow dynamics when the motion becomes continuous: the successive clumps do not merge even if their motion overlaps in time. According to the arguments advanced by Rajchenbach [17], the characteristic fall time of the grains is thus the same in the avalanching and the continuous flow. Therefore we observe no hysteresis.

The phase diagram

We summarize our measurements of the different flow regimes in a phase diagram (Fig. 12) indicating the nature of the flow as a function of liquid content and rotation rate. Each symbol corresponds to a measurement, grey symbols denote avalanches, black symbols denote continuous flow, white symbols mark the hysteretic regions. The most complete graph corresponds to the large, $d = 0.9\,\mathrm{mm}$, beads (Fig. 12(a)). Here the three regimes are clearly visible. Near $\tau \approx 0.02\,\%$ the disappearance of hysteresis and the displacement of the transition point towards higher rotation rates indicates the transition from the granular to the correlated regime. The sudden change in the transition point around $\tau \approx 0.1\,\%$ marks the onset of the viscoplastic continuous flow.

The other two diagrams (Fig. 12(b) and (c), medium ($d = 0.5\,\mathrm{mm}$) and small ($d = 0.35\,\mathrm{mm}$) beads, respectively) contain fewer points, but the main trends are visible. A universal feature of the phase diagrams is that, upon approaching the correlated regime from the granular one the transition point moves towards higher rotation rates. This suggests that the clump formation leads to more effective transport and quicker avalanches as was noted in our previous draining crater studies [10]. A general trend is that for smaller beads the transition to correlated behavior occurs at higher liquid contents, most probably due to the larger internal surface of these samples.

The most striking feature is that, as the bead size is decreased, the viscoplastic behavior and in particular the region of the viscoplastic continuous flow diminishes. For the $d = 0.5\,\mathrm{mm}$ beads it is restricted to the region between $0.3\,\% \lesssim \tau \lesssim 0.8\,\%$ and $1\,\mathrm{rpm} \lesssim \Omega \lesssim 10\,\mathrm{rpm}$, and the $d = 0.35\,\mathrm{mm}$ beads exhibit no viscoplastic flow at all. A possible explanation is that, in samples consisting of smaller beads, the number of contacts at the boundary of a given volume of material is much larger, therefore the cohesive forces dominate inertial effects. For smaller beads the hysteresis of the continuous-to-avalanche transition also seems to decrease, but this is difficult to interpret and will require further investigation to understand.

We have performed some preliminary measurements on the role of the viscosity of the interstitial liquid. The results (not shown here) indicated that the fluid viscosity is indeed an important parameter, e.g. experiments with a highly viscous silicon oil yielded viscoplastic flow in a wider range of liquid contents and rotation rates. These results are also consistent with the findings of Samandani and Kudrolli [9].

SURFACE MORPHOLOGY

Up to this point we have described the surface by a single quantity, the overall surface angle, but the actual surfaces are rough and have significant curvature. This morphology contains additional information about the system, and should be useful in producing realistic models of wet granular flow. Fig. 13 shows sample surface profiles for various materials. The graph confirms that the wet samples form exotic surfaces, especially for the smaller beads. Note that, besides the overall shape of the surface, some smaller scale roughness is also observable for the larger liquid contents. These small scale features typically are random and fluctuate between avalanches. In the viscoplastic regime, however the coherence of the flow strongly reduces fluctuations, and a robust pattern is formed that is reproduced at the end of each avalanche (as discussed in section below).

Since the surfaces of the largest ($d = 0.9\,\mathrm{mm}$) bead samples are relatively simple, we investigate them in more detail. Fig. 14 shows sample surfaces for the $d = 0.9\,\mathrm{mm}$ beads at various liquid contents and rotation rates. In the granular regime the surface is almost flat, correlated avalanches typically form concave surfaces, and the viscoplastic flow typically results in a convex surface. Furthermore, at the highest rotation rates, the surface is S-shaped due to inertial effects across the entire wetness range [17]. The convexity of the surface can be characterized quantitatively several ways [37]. A simple and robust measure is the integrated area (κ) between the surface profile ($h(x)$) and the straight line connecting the two ends of the surface line. For a flat surface where $h(x)$ is a straight line, $\kappa = 0$; $\kappa < 0$ im-

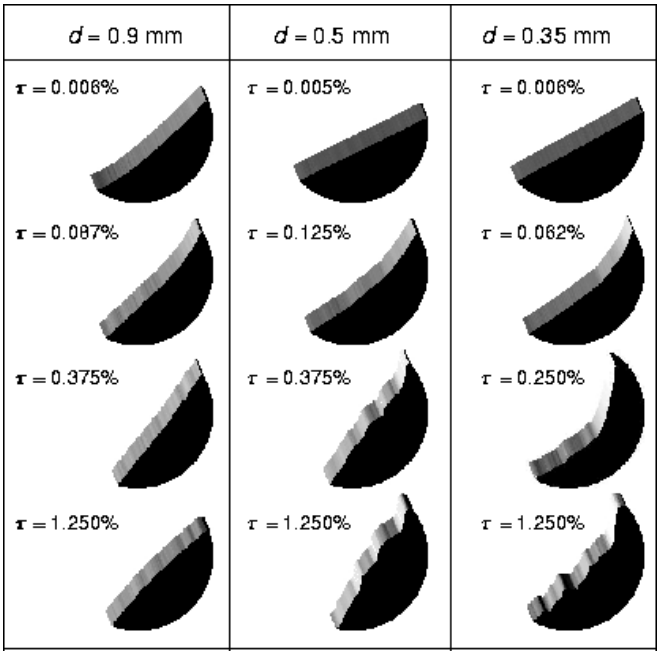


FIG. 13: *This is a reduced resolution figure* [22]. Sample surfaces for various materials, as indicated in the figure. The snapshots were taken right before an avalanche, the rotation rate was $\Omega = 0.05\,\mathrm{rpm}$ for the large and medium beads and $\Omega = 0.043\,\mathrm{rpm}$ for the small beads. Note that the surface is close to flat in the granular regime, mostly concave in the correlated regime and mostly convex in the viscoplastic regime. Note also the smaller scale structure at the smaller bead sizes.

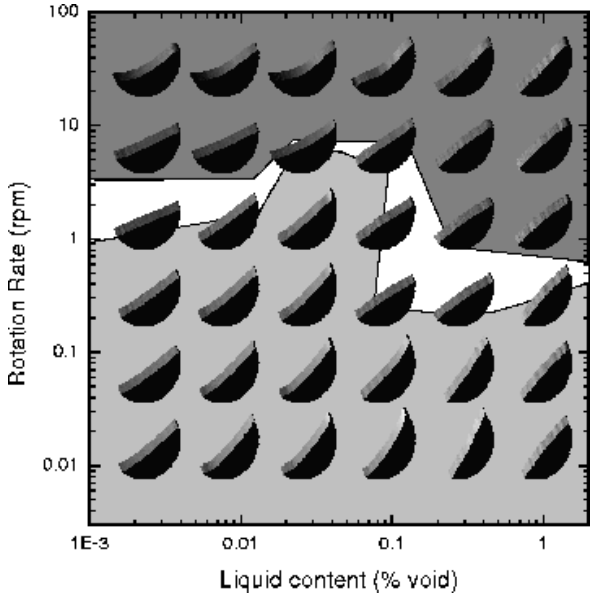


FIG. 14: *This is a reduced resolution figure* [22]. Shape of the surface at various points of the parameter space for the large, $d = 0.9\,\mathrm{mm}$ beads. A sketch of the phase diagram is shown in greyscale in the background: the dark grey region denotes continuous flow, the light grey region corresponds to avalanches; the white area is the hysteretic regime. The shape changes both as a function of Ω and τ. At the highest rotation rates the S-shaped regime [17] is clearly observable.

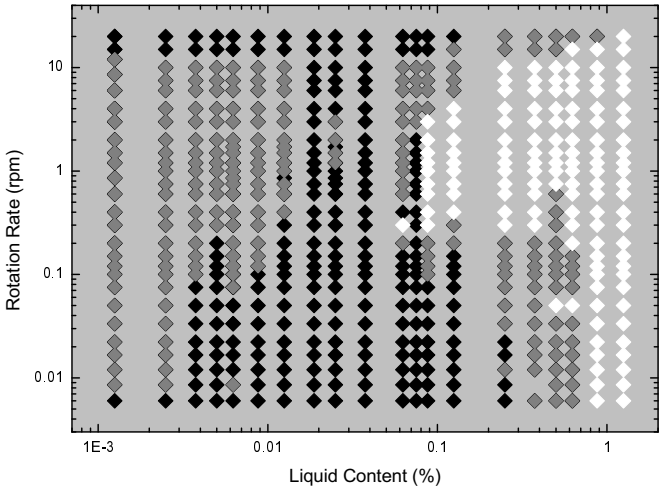


FIG. 15: The value of convexity parameter κ as a function of the rotation rate and the liquid content for the large beads, $d = 0.9\,\mathrm{mm}$. Black symbols: concave surface ($\kappa < 0$), white symbols: convex surface ($\kappa > 0$), grey symbols: ($\kappa \approx 0$).

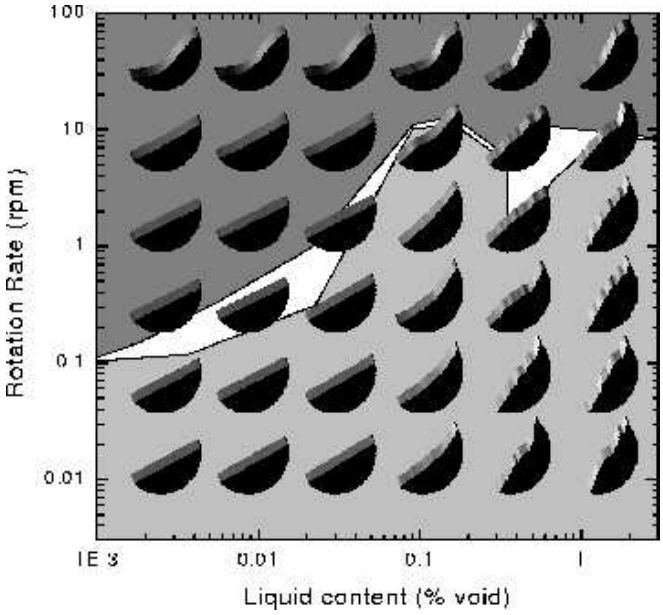


FIG. 16: *This is a reduced resolution figure* [22]. Shape of the surface at various points of the parameter space, for the medium, $d = 0.5\,\mathrm{mm}$ beads (see the caption of Fig. 14 for further explanation). The observed surface shapes are more complicated for these beads compared to the $d = 0.9\,\mathrm{mm}$ beads, but the overall convex vs. concave nature is similar.

plies a predominantly concave surface, $\kappa > 0$ implies a predominantly convex surface.

In Fig. 15 the value of κ is indicated by the color of symbols as a function of τ and Ω. Black symbols correspond to concave surfaces (negative κ), and approximately indicate the correlated regime. White symbols are used for positive κ values, corresponding to the viscoplastic regime. Grey symbols indicate that $\kappa \approx 0$, either because the surface is flat (upper left region of Fig. 15 - this is approximately the granular regime), or because convex and concave parts are balanced (at the boundary of correlated and viscoplastic regimes). For comparison we also show the typical observed surface shapes for the medium size ($d = 0.5\,\mathrm{mm}$) beads (Fig. 16). Also here the convexity of the surface seems to correlate with the different flow regimes, however, some additional smaller scale features are also observable.

Clearly, the phase boundaries in Fig. 15 are not vertical lines. This means that the liquid content is not the only parameter influencing the behavior: changing the rotation rate can also switch between different flow mechanisms. This observation implies that the formation of correlated clumps is a dynamical process with characteristic times comparable to the other timescales of the experiment. We expect that the different convexity in the different regimes could be reproduced relatively easily in the framework of a continuum model. A detailed explanation of the surface shapes, however, would probably require a full analysis of the avalanche dynamics.

DETAILED DYNAMICS OF AVALANCHES

The rotating drum apparatus allows us to obtain information not just about the medium before and after the avalanche events, but also about the details of the grain motion *during avalanche events*. In order to analyze the dynamics of avalanches we have obtained two-dimensional space-time matrices, $h(x,t)$, characterizing the sample surfaces throughout the avalanche process which can then be analyzed to produce a variety of information about the individual avalanches. By taking derivatives of the $h(x,t)$ data, we obtain the local angle, $\alpha(x,t) = \arctan[\partial_x h(x,t)]$, and the local vertical velocity, $u(x,t) = \partial_t h(x,t)$, of the surface profile. Furthermore, by then integrating the vertical velocity (using the continuity equation and assuming constant density [38]), we also obtain the local flux in the avalanche, i.e. $\phi(x,t) = \rho w \int_{-D/2}^{x} \partial_t h(x',t) dx'$ (where ρ is the grain density, w is the width of the drum, and D is the drum diameter), which represents the material flowing through a given vertical plane at position x. In Fig. 17(a) we present snapshots of the progression of single avalanches for several typical liquid contents. Fig. 17(b) displays $\alpha(x,t)$ as a function of space (horizontally) and time (downwards) for the same individual avalanches. In Fig. 17 (c-e), we present the average behavior of $300 - 500$ avalanches at the same liquid contents, and show similar graphs of the time evolution of $\langle\alpha(x,t)\rangle$, $\langle u(x,t)\rangle$, and $\langle\phi(x,t)\rangle$, where $\langle\rangle$ denotes averaging over avalanches. By obtaining these quantitative measures of the averaged properties, we can separate the robust characteristics of the avalanche dynamics from the large fluctuations which

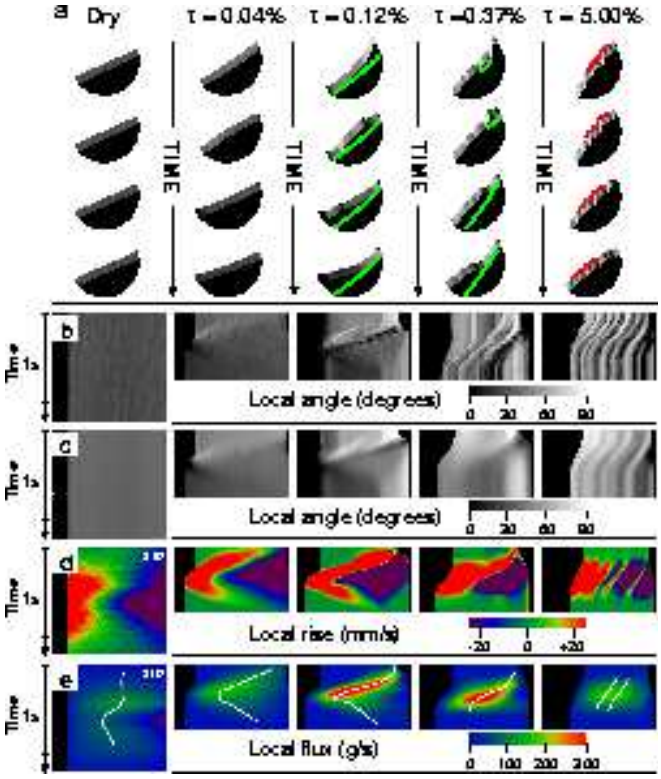


FIG. 17: *This is a reduced resolution figure* [22]. (color) Dynamics of avalanches of different types with grain size $d = 0.5\,\mathrm{mm}$, at $\Omega = 0.12\,\mathrm{rpm}$. (a) Snapshots (at $0.1 - 0.2\,\mathrm{s}$ time intervals) of five single avalanches corresponding to different liquid contents. The third dimension is used for a brightness-coded representation of the local slope (α). The green lines indicate approximate slip planes in the correlated regime, and the red line shows the traveling quasi-periodic surface features in the viscoplastic regime. (b) The local slope with the same brightness coding, as a function of space and time. A horizontal line corresponds to a surface profile at a given instant, and time increases downwards (thus avalanches propagate down and to the left). The slanted bright and dark regions correspond to the avalanche front and the kink respectively (see text). The stripes at higher liquid contents indicate lasting surface features. (c) (d) (e) The characteristic features of the avalanches averaged over $300 - 500$ avalanche events. The displayed quantities are (c) the local surface angle, (d) the rate of change of local height, and (e) the local grain flux (the white lines indicate the point of maximum current), respectively. Note that the surface patterns at the highest oil contents are robust against averaging.

are inherent in avalanche processes.

The averaging process raises a few technical questions. First, the order of averaging and numerical differentiation is optional, i.e. we can either calculate $\alpha(x,t)$ and the other quantities from the raw $h(x,t)$ data and perform averaging afterwards, or take the averaged $\langle h(x,t)\rangle$ and calculate its numerical derivatives. We verified that the two methods yield equivalent results, and chose the former option.

A second question is how to find the corresponding frames in different recorded avalanches. In order to make this question clear let us consider the averaging in more detail. Let us suppose that we have recorded the variation of the surface profile for N avalanches, and we have N matrices $h^{(i)}_{u,v}$, $i = 1..N$ denoting the local height in the ith avalanche at the position $x = -D/2 + u\,\delta x$ and time $t = t^{(i)}_0 + v\,\delta t$, where δx and δt are the spatial and temporal resolutions respectively, and $t^{(i)}_0$ is "the starting time" of the ith avalanche. Then, to obtain the average behaviour, we calculate $\langle h_{u,v}\rangle = \sum_{i=1}^{N} h^{(i)}_{u,v}/N$. Since the properties of the avalanches (e.g. duration) vary between avalanche events, the appropriate choice for $t^{(i)}_0$ is not trivial. We tried several algorithms and then decided to use the most robust one which was based on the variation of the overall surface angle $\theta(t)$. We fitted straight lines to the segments of the sawtooth signal of $\theta(t)$ (see Fig. 3), and calculated the time $t^{(i)}_{int}$ corresponding to the intersection of the straight lines at the beginning of an avalanche. Then we chose $t^{(i)}_0 = t^{(i)}_{int} - 0.5\,\mathrm{sec}$.

A third problem arises from the fact that the $h^{(i)}_{u,v}$ matrices have empty elements: the surfaces do not extend from $-D/2$ to $D/2$. Simply excluding the empty elements from the averaging leads to the appearance of some artifacts at the edges. To resolve this issue, we filled in the empty elements with the value of the closest elements in that row (as if the surface continued horizontally over the edge of the drum), performed the averaging, and then cut down those parts of the averaged profile that were outside the drum. Note that this procedure only influenced the behavior very close to the edges of the sample.

In Fig. 18 we present the same data as series of curves, where the columns again represent different liquid contents. In the first row of graphs we plot the averaged surface profiles ($\langle h(x)\rangle$) at different time instants during the avalanche. The second row of graphs shows the variation of the local angle ($\langle \alpha(x)\rangle$), and the third row plots the local flux ($\langle \phi(x)\rangle$) with triangles showing the position of maximum flux. In the following we analyze the dynamics in the 3 regimes based on Figs. 17 and 18. We have also magnified parts of Fig. 17 in Fig. 19 to emphasize particular features in the data. For comparison we also show the most important avalanche types for the $d = 0.9\,\mathrm{mm}$ beads in Fig. 20. Apart from the absence of robust large-scale patterns for the $d = 0.5\,\mathrm{mm}$ beads (discussed below), the qualitative features of the avalanches are quite similar for the two types of beads although the effects are less pronounced for the $d = 0.9\,\mathrm{mm}$ beads.

The avalanche types

Granular avalanches. With dry grains [13, 17, 18, 29, 30, 35], the surface remains almost flat throughout the avalanche, and the avalanches have a much longer dura-

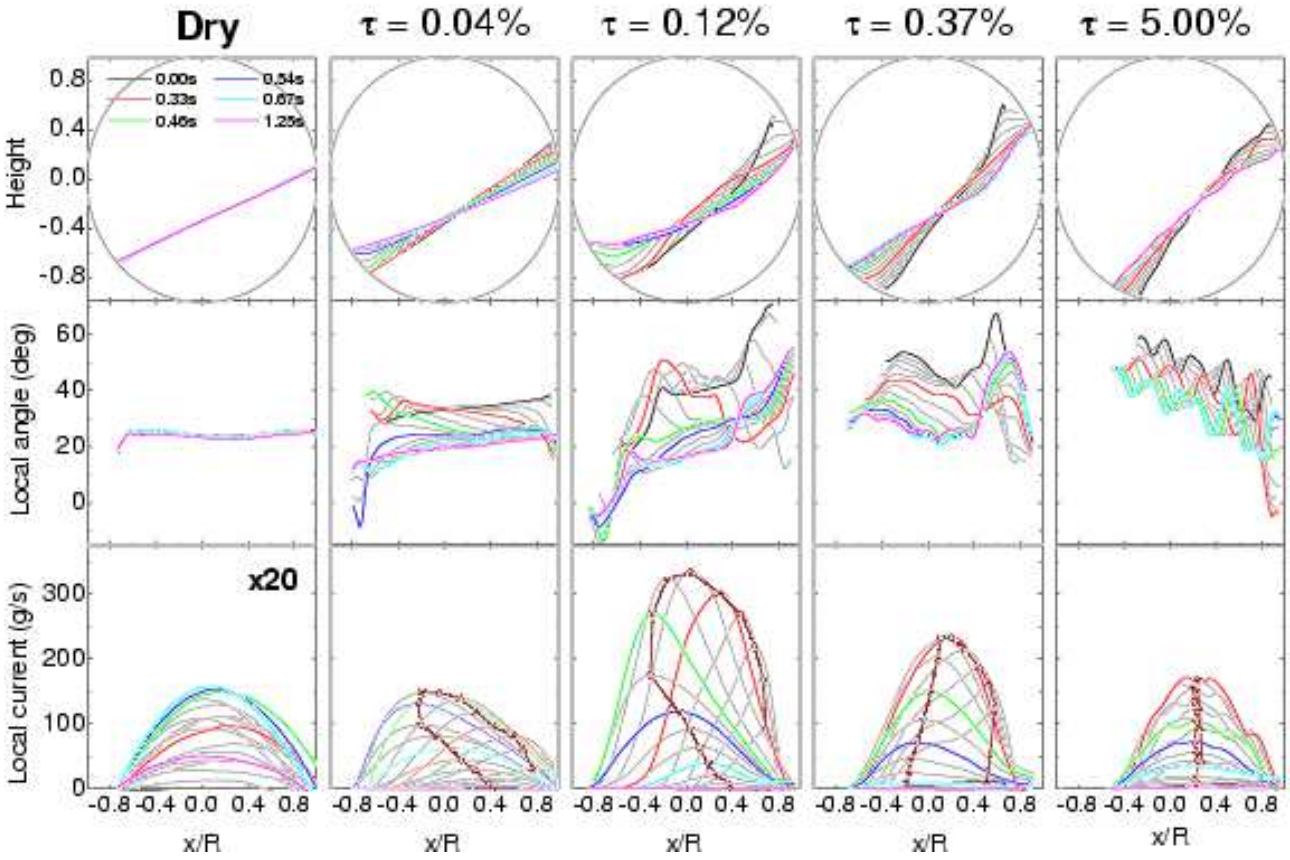


FIG. 18: *This is a reduced resolution figure* [22]. (color) Averaged dynamical parameters: $\langle h(x)\rangle$, $\langle \alpha(x)\rangle$, and $\langle \phi(x)\rangle$ as a function of space at various time instants during the avalanche for 5 different liquid contents, $d = 0.5\,\mathrm{mm}$, $\Omega = 0.12\,\mathrm{rpm}$. The time interval between successive curves is 0.066 sec, some curves are marked with color as specified in the legend. In the lowest row, triangles mark the point of maximum current. The most important features for different oil contents are the following. *Dry samples.* The avalanches are very small, and our resolution is insufficient to resolve the detailed dynamics. $\tau = 0.04\,\%$ *Granular regime.* The surface is close to flat, but the local angle is somewhat larger near the top of the slope. The dynamics is dominated by fronts of rolling grains. The region of steeper slope corresponding to the downward propagating front as well as the negative slope of the kink is visible in the graph of the local angle. The point of maximum current also moves downhill then uphill due to the fronts. $\tau = 0.12\,\%$ *Correlated regime*: failure occurs along a slip plane and a block slides down. The block is best seen in the red curve, the edges are smoothed by the averaging over several hundred avalanches. Some rolling grains are still present, as marked by the presence of the kink. $\tau = 0.37\,\%$ Correlated regime, usually with multiple avalanches, but these are averaged out. The fronts have disappeared, and the angle near the bottom of the slope decreases monotonically. There are lasting contacts during the avalanche, thus the grains cannot roll, and the material stops coherently as a block when it reaches the bottom. $\tau = 5.00\,\%$ *Viscoplastic regime.* The surface moves coherently. The current extends over the whole surface during the whole duration of the avalanche. Curves of the local angle reveal the robust surface patterns as a series of local maxima. During the avalanche the local maxima move downwards (and spread out slightly), and a new maximum is formed near the top.

tion and much smaller flux than in the wet media - as is expected due to the lack of cohesion. Our resolution is not sufficient to distinguish any propagating front in this case, but our system is very similar to that investigated by [12], all the surface grains are close to the limit of their stability. Thus we assume that the failure mechanism is similar: the propagation of the front destabilizing the grains is quicker than the material flow. This type of front is marked only by a very slight dilation of the material, which we cannot detect.

With the addition of very small amounts of liquid (e.g. $\tau = 0.04\,\%$, see Fig. Fig. 19(a)) the avalanches become much larger due to the onset of intergrain cohesion — this allows us to observe the dynamics in more detail. In this granular regime the avalanche is always initiated at the top of the surface, and the upper part of the surface is quickly destabilized. As the particles start moving downwards, a front of rolling grains travels downhill. The grains in the lower regions remain at rest until the rolling grains reach them. This type of front corresponds to the "start down" front of Douady et al. [39]. The difference in behavior compared to the perfectly dry material can

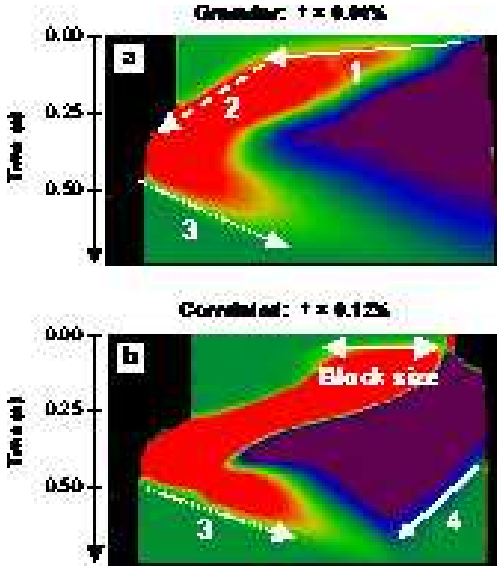


FIG. 19: *This is a reduced resolution figure* [22]. (color) The various fronts observed in our setup in (a) the granular regime ($\tau = 0.04\,\%$) and in (b) the low liquid content region of the correlated regime ($\tau = 0.12\,\%$), for $d = 0.5\,\mathrm{mm}$, $\Omega = 0.12\,\mathrm{rpm}$. The colors indicate the rate of change of local height during the avalanche (see Fig. 17). We observe 4 different fronts. 1: destabilizing front. Propagates faster than the material flow via interactions between neighboring grains — destabilizes particles. 2: Avalanche front. Consists of rolling grains, which proceed on a medium at rest and destabilize particles by collisions. 3: Kink. The rolling grains accumulate at the lower wall and form a region of low slope there. This slows down the incoming grains, thus this front travels uphill. 4: Rear front. The moving grains leave the static ones behind.

probably be explained by the slight concave curvature of the surface: the grains lower on the slope are in a relatively stable state when the avalanche is initiated.

When the downward-propagating front reaches the wall of the drum at the bottom of the slope, a kind of shockwave is formed, and the rolling of grains is stopped by a region of smaller local angle travelling uphill. The second front is classified as a "stop up" front by [39], and corresponds to the "kink" seen in other experiments on dry beads (generally associated with individually rolling grains reaching a solid barrier at the bottom of the slope [40, 41, 42]).

Correlated Avalanches. At intermediate liquid contents, in the correlated regime ($0.1\,\% < \tau < 2\,\%$), the principal failure mechanism is a fracture along a curved slip plane (approximated by the green lines in Fig. 17(a)), analogous to the dynamics of a class of geological events known as "slides" [43]. This is the failure mechanism described by the Mohr-Coulomb model [1, 4]. At $\tau = 0.12\,\%$ there is a single slip plane, but at larger liquid contents ($\tau = 0.37\,\%$) the avalanches occur through a succession of local slip events. The medium becomes more cohesive with increasing liquid content, preventing grains from moving individually, and thus the kink disappears for $\tau \geq 0.3\,\%$ since the material moving as a connected block stops coherently when it hits the bottom.

Viscoplastic Avalanches. The onset of the viscoplastic regime ($\tau \approx 2\,\%$) is accompanied by dramatic changes in the behavior. The flow becomes correlated across the entire granular surface as demonstrated by the parallel lines during the avalanche in Fig. 17 (b) and (b). Since the whole surface moves coherently (rather than breaking apart and evolving separately in different parts of the surface), fluctuations are strongly suppressed [10]. This behavior is qualitatively similar to a different class of geological event, called a "debris flow" or "mudflow" [43, 44, 45]. The coherent nature of the motion in this regime leads to novel aspects of the dynamics which are not observed in other granular systems.

Pattern formation in the viscoplastic regime

One novel property of the viscoplastic avalanches is the robust topology of the top surface which spontaneously forms a nearly periodic pattern (seen in Fig. 17(a)). This surface structure is maintained essentially intact during the avalanche (note that the lines are continuous throughout the avalanche in Fig. 17(b)), indicating that there are lasting contacts in the flowing layer. Moreover, the pattern is not random, but rather has features which are reproduced at the end of each avalanche. This is demonstrated most clearly in Fig. 18 and in Fig. 17(b), where the average of 347 avalanches of the $\tau = 5\,\%$ sample has the same features as the typical individual avalanche shown in Fig. 17(a) and (b). The robust nature of the surface structure of the wettest grains is in sharp contrast to the other regimes where averaging completely smoothes out the smaller surface features. We can understand this behavior as resulting from coherence of the entire flow, which strongly reduces fluctuations in this regime. With minimal fluctuations, the final surface structure after each avalanche is essentially the same, thus setting the same initial condition for the next avalanche. With the same initial conditions for each avalanche, naturally the surface features are reproduced each time.

Our experiments with the larger ($d = 0.9\,\mathrm{mm}$) beads also reveal some pattern formation (see Fig. 20(b)), but with a smaller characteristic size corresponding to $8 - 10$ grain diameters. The difference is probably due to the smaller ratio of the cohesive forces to the gravitational forces on the grains. Due to the small length scale of these patterns, they are largely averaged out, but we have also observed robust patterns that are repeated after each avalanche under several different sets of conditions (see e.g. Fig. 20, $\tau = 0.375\,\%$) (these other patterns are not

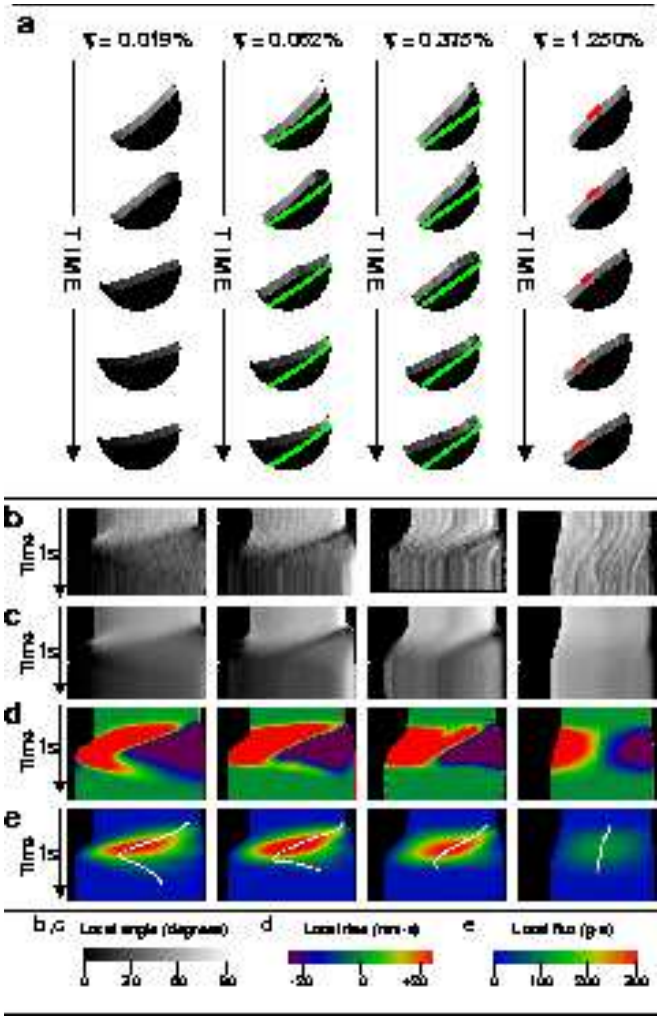


FIG. 20: *This is a reduced resolution figure* [22]. (color) Avalanche dynamics in samples consisting of large beads $d = 0.9\,\mathrm{mm}$. (See also the caption of Fig. 17.)

as periodic as at $\tau = 5\,\%$, $d = 0.5\,\mathrm{mm}$). The dependence of the pattern on grain size and other factors will be the subject of a future investigation.

DYNAMIC PROPERTIES OF CONTINUOUS FLOWS

In the previous section we demonstrated that the avalanche dynamics are dramatically different in the three regimes of behavior. The different dynamics are also evident at higher rotation rates where the flow is continuous. In this section we compare the properties of the continuous flow in the three wetness regimes, with special attention to the viscoplastic flow. Here we only examine the $d = 0.9\,\mathrm{mm}$ beads, since they exhibit viscoplastic continuous flow in the widest range of parameter space.

Fig. 21 shows the evolution of the surface profile during

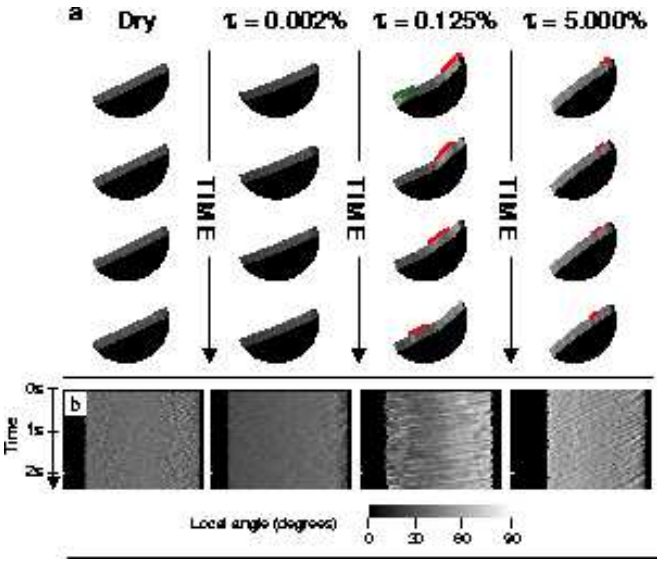


FIG. 21: *This is a reduced resolution figure* [22]. (color) Comparison of the types of continuous flow at $\Omega = 10\,\mathrm{rpm}$ (large beads: $d = 0.9\,\mathrm{mm}$). (a) snapshots at time intervals of 0.067 s. The red marks indicate travelling surface features. (b) time evolution of the surface angle $\alpha(x,t)$. The travelling surface features appear as stripes.

different types of continuous flow for $\Omega = 10\,\mathrm{rpm}$. In the granular regime (e.g. $\tau = 0$ and $0.002\,\%$) the surface profile is practically a straight line with only noise-like variations. Our resolution is insufficient to resolve the individually rolling grains. By contrast, in the correlated regime the surface is clearly concave, and the flow consists of a succession of clumps moving downhill. From the slope of the stripes in 21(b) we can estimate the velocity of the moving clumps: $v \approx 50 - 60\,\mathrm{cm/s}$. In the viscoplastic regime the flow is smooth again, and the travelling surface features demonstrate that there are lasting contacts in the flowing layer. The slopes of stripes indicate that the flow is much slower in this regime, $v \approx 10 - 15\,\mathrm{cm/s}$. We note that the rotation rate is the same for all the presented liquid contents, meaning that the material flux is constant. The difference in surface velocity thus presumably indicates that the moving layer is much deeper in case of viscoplastic flow.

In order to compare the viscoplastic flow to the ordinary granular flow, we added some tracer particles to measure the surface velocity v more accurately as a function of rotation rate, Ω (Fig. 22). The viscoplastic flow is slower by a factor of two than the granular one, and more importantly, the two curves correspond to rather different functional forms. The curvature of the granular curve suggest that at higher rotation rate the flow depth is increased, as has been previously suggested [46]. Naturally in our finite setup the flow depth cannot in-

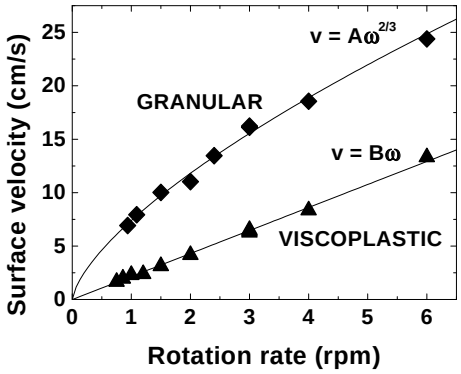


FIG. 22: The velocity v at the surface as a function of rotation rate Ω for the ordinary granular and the viscoplastic continuous flow (large beads, $d = 0.9\,\mathrm{mm}$, the liquid contents are $\tau = 0.005\,\%$ and $\tau = 0.25\,\%$ respectively). The continuous lines represent power-low fits to the data. The linear curve for the viscoplastic flow indicates that flow depth is independent of the rotation rate.

crease infinitely which may explain why our measured $v(\Omega)$ deviates from $\Omega^{1/2}$ which would be expected from a linear velocity profile [46, 47, 48]. On the other hand, the recent work of Aranson et al. actually predicts a 2/3 power law [49, 50]. The linear $v(\Omega)$ for viscoplastic flow suggests a *constant flow depth* which is independent of the flow rate. This observation is consistent with the coherent nature of this type of flow: the flow depth is not determined by local mechanisms [12], but is fixed by the geometry of the whole system. In order to characterize the viscoplastic flow in greater detail and check whether the flow depth is really constant we have performed explicit measurements to determine the extent and shape of the flowing layer. The results confirmed that the flow depth is almost independent of the rotation rate [23].

CONCLUSIONS

We have investigated many features of the dynamic behavior of wet granular samples in a rotating drum. We found that all these features are related and in particular all of them reflect the 3 fundamental regimes observed earlier [10].

In the granular regime the cohesive forces are relatively small, and they have almost no effect in the fluidized flowing layer. Thus only a small increase is observable in $\theta_{\max}$, while θ_r hardly changes. The grains are rolling freely, and avalanche dynamics is dominated by propagating fronts. These form nearly flat surfaces resulting in relatively small avalanche size fluctuations. At high rotation rates we observe continuous flow with a fluidized flowing layer, similarly to surface flows in dry samples.

On the other hand, in the correlated regime the grains stick together and form clumps. The increased cohesion leads to a large increase in $\theta_{\max}$ and θ_r. As the free rolling of grains becomes impossible, the avalanche fronts disappear and steep, rugged, and usually concave surfaces are formed. Variations of the surface shape lead to wide avalanche size distributions. In this regime the continuous flow consists of a succession of falling clumps, thus the hysteresis between avalanching and continuous flow disappears.

Finally, in the viscoplastic regime the flow becomes coherent over the entire sample, and $\theta_{\max}$ and $\Delta\theta$ decrease slightly due to lubrication and viscous effects. The reduced fluctuations lead to narrower avalanche size distributions and the formation of robust patterns that are reproduced at the end of each avalanche. The transition to continuous flow happens at relatively low rotation rates, and the hysteresis reappears. The coherence of the viscoplastic continuous flow is manifested in traveling surface features and a velocity independent flow depth.

While the flows we observe appear to have analogies with geological events, it is important to note that real geological materials usually consist of polydisperse irregular particles often with very high ($\tau \approx 100\%$) water contents and that the scaling of our system to geological lengthscales is non-trivial (indeed, based our on earlier work we expect that all of the results will be affected by the size of the container [10]). Furthermore, avalanche studies in real soil have demonstrated additional phenomena associated with soil saturation [51]. Interestingly we still recover some of the basic dynamical processes in our model system, which should aid the description of qualitatively different flow behaviors in the framework of a single model [20, 52].

The changes in the dynamic behavior with wetting are associated with the increasingly coherent nature of the flow, i.e. the formation of coherently moving clusters – clumps – due to the increased cohesion and viscous effects. Within a cluster, local velocity fluctuations should be suppressed, and thus the local granular temperature ($T = \langle v^2 \rangle - \langle v \rangle^2$) should approach zero, but the clusters themselves both form and break apart during an avalanche process in a finite container. An important theoretical question raised by our data is how a length scale describing the size of the clumps may emerge from a granular flow model, and how such a length scale would vary with the type of media, the total size of the granular sample, the nature of intergranular adhesion, viscosity of the fluid, and the type of granular flow. While the present experiments have raised these questions, further experimental studies expanding the investigated phase space as well as computational modelling will almost certainly be necessary before a complete understanding is approachable.

We gratefully acknowledge helpful discussions with J. Banavar, A.-L. Barabási, and Y. K. Tsui. We are also grateful for support from the Petroleum Research Fund and NASA Grant NAG3-2384. P. T. and T. V. are

grateful for the partial support from OTKA Grant No. T033104.

[1] R. M. Nedderman, *Statics and Kinematics of Granular Materials* (Cambridge Univ. Press., Cambridge, 1992).

[2] R. Albert, I. Albert, D. Hornbaker, P. Schiffer, and A.-L. Barabási, Phys. Rev. E **56**(6), R6271 (1997).

[3] D. J. Hornbaker, R. Albert, I. Albert, A.-L. Barabási, and P. Schiffer, Nature **387**, 765 (1997).

[4] T. C. Halsey and A. J. Levine, Phys. Rev. Lett. **80**, 3141 (1998).

[5] T. G. Mason, A. J. Levine, D. Ertas, and T. C. Halsey, Phys. Rev. E **60**, 5044 (1999).

[6] L. Bocquet, E. Charlaix, S. Ciliberto, and J. Crassous, Nature **396**, 735 (1998).

[7] N. Fraysse, H. Thomé, and L. Petit, in *Powders & Grains 97*, edited by R. P. Behringer and J. T. Jenkins (A.A. Balkema, Rotterdam, 1997).

[8] A. Samadani and A. Kudrolli, Phys. Rev. Lett. **85**, 5102 (2000).

[9] A. Samadani and A. Kudrolli, Phys. Rev. E. **64**, 051301 (2001).

[10] P. Tegzes, R. Albert, M. Paskvan, A.-L. Barabási, T. Vicsek, and P. Schiffer, Phys Rev E. **60**, 5823 (1999).

[11] P. Tegzes, T. Vicsek, and P. Schiffer, Phys Rev Lett (In Press).

[12] J. Rajchenbach, Phys. Rev. Lett. **88**, 014301 (2002).

[13] A. Daerr and S. Douady, Nature **399**, 241 (1999).

[14] G. A. Held, D. H. Solina, D. T. Keane, W. J. Haag, P. Horn, and G. G. Grinstein, Phys. Rev. Lett. **65**(9), 1120 (1990).

[15] P.-A. Lemieux and D. Durian, Phys. Rev. Lett. **85**, 4273 (2000).

[16] L. C. Jia, P.-Y. Lai, and C. K. Chan, Physica A **281**, 404 (2000).

[17] J. Rajchenbach, Phys. Rev. Lett. **65**(18), 2221 (1990).

[18] C. Liu, H. M. Jaeger, and S. R. Nagel, Phys. Rev. A **43**(12), 7091 (1991).

[19] N. Fraysse, H. Thomé, and L. Petit, European Phys. J. B **11**, 615 (1999).

[20] S. T. Nase, W. L. Vargas, A. A. Abatan, and J. J. McCarthy, Powder tech. **116**, 214 (2001).

[21] M. A. S. Quintanilla, J. M. Valverde, A. Castellanos, and R. E. Viturro, Phys. Rev. Lett. **87**, 194301 (2001).

[22] The original figures and videos of avalanches are available at the following URL: `http://angel.elte.hu/~tegzes/condmat.html\#ava_long`.

[23] P. Tegzes, Ph.D. thesis, Eötvös University, Budapest (2002), URL `http://angel.elte.hu/~tegzes/thesis.html`.

[24] S. Nasuno, A. Kudrolli, and J. P. Gollub, Phys. Rev. Lett. **79**, 949 (1997).

[25] I. Albert, P. Tegzes, B. Kahng, R. Albert, J. Sample, M. Pfeifer, A.-L. Barabasi, T. Vicsek, and P. Schiffer, Phys. Rev. Lett **84**, 5122 (2000).

[26] I. Albert, P. Tegzes, R. Albert, J. G. Sample, A.-L. Barabási, T. Vicsek, B. Kahng, and P. Schiffer, Phys. Rev. E **64**, 031307 (2001).

[27] R. G. Cain, N. W. Page, and S. Biggs, Phys. Rev. E **64**, 016413 (2001).

[28] P. Bak, C. Tang, and K. Wiesenfeld, Phys. Rev. Lett. **59**(4), 381 (1987).

[29] M. Bretz, J. B. Cunningham, P. Kurczynski, and F. Nori, Phys. Rev. Lett. **69**(16), 2431 (1992).

[30] V. Frette, K. Christensen, A. Malthe-Sørenssen, J. Feder, T. Jøssang, and P. Meakin, Nature **379**, 49 (1996).

[31] P. Evesque, Phys. Rev. A **43**, 2720 (1991).

[32] G. Baumann and D. E. Wolf, Phys. Rev. E **54**, R4504 (1996).

[33] W. Losert, J.-C. Géminard, S. Nasuno, and J. P. Gollub, Phys. Rev. E **61**, 4060 (2000).

[34] C. Caponeri, S. Douady, S. Fauve, and S. Laroche, in *Mobile Particulate Systems*, edited by E. Guazelli and L. Oger (Kluwer, Dordrecht, 1995), p. 331.

[35] H. M. Jaeger, C. Liu, and S. R. Nagel, Phys. Rev. Lett. **62**(1), 40 (1989).

[36] V. G. Benza, F. Nori, and O. Pla, Phys. Rev. E **48**, 4095 (1993).

[37] A. D. C. Smith, P. G. Batchelor, X. A. Chitnis, D. L. G. Hill, and T. Sharma, Schizophrenia Research **41**, A217 (2001).

[38] S. Douady, B. Andreotti, and A. Daerr, Euro. Phys. J. B **11**, 131 (1999).

[39] S. Douady, B. Andreotti, A. Daerr, and P. Clade, in *Powders & Grains 2001*, edited by Kishino (Swets & Zeitlinger, Lisse, 2001), pp. 443–446.

[40] H. A. Makse, S. Havlin, P. R. King, and H. E. Stanley, Nature **386**, 379 (1997).

[41] J. M. N. T. Gray and Y. C. Tai, in *Physics of Dry Granular Media*, edited by H. J. Herrmann, J.-P. Hovi, and S. Luding (Kluwer, Dordrecht, 1998), pp. 697–702.

[42] P. Cizeau, H. A. Makse, and H. E. Stanley, Phys. Rev. E **59**, 4408 (1999).

[43] R. Dikau, D. Brunsden, L. Schrott, and M.-L. Ibsen, *Landslide Recognition* (Wiley, Chichester, 1996).

[44] R. M. Iverson, Rev. Geophys. **35**, 245 (1997).

[45] P. Coussot, *Mudflow rheology and dynamics* (A. A. Balkema, Rotterdam, 1997).

[46] D. Bonamy, B. Faucherand, M. Planelle, F. Daviaud, and L. Laurent, in *Powders & Grains 2001*, edited by Kishino (Swets & Zeitlinger, Lisse, 2001), pp. 463–466.

[47] J. Rajchenbach, in *Physics of Dry Granular Media*, edited by H. J. Herrmann, J.-P. Hovi, and S. Luding (Kluwer, Dordrecht, 1998).

[48] K. Yamane, M. Nakagawa, S. A. Altobelli, T. Tanaka, and Y. Tsuji, Phys. Fluids **10**, 1419 (1998).

[49] I. S. Aranson and L. S. Tsimring, Phys. Rev. E **65**, 061303 (2002).

[50] I. Aranson (2002), personal communication.

[51] R. M. Iverson, M. E. Reid, N. R. Iverson, R. G. LaHusen, M. Logan, J. E. Mann, and D. L. Brien, Science **290**, 513 (2000).

[52] J. M. N. T. Gray, J. Fluid Mech. **441**, 1 (2001).